Performance of Metal-Catalyzed Hydrodebromination of Dibromomethane Analyzed by Descriptors Derived from Statistical Learning

A. J. Saadun,[§] S. Pablo-García,[§] V. Paunović, Q. Li, A. Sabadell-Rendón, K. Kleemann, F. Krumeich, N. López,* and J. Pérez-Ramírez*

ABSTRACT: The catalyzed semihydrogenation of dibromomethane (CH_2Br_2) to methyl bromide (CH_3Br) is a key step in the bromine-mediated upgradation of methane. This study presents a cutting-edge strategy combining density functional theory (DFT), catalytic tests complemented with the extensive characterization of a wide range of metal catalysts (Fe, Co, Ni, Cu, Ru, Rh, Ag, Ir, and Pt), and statistical tools for a computer-assisted investigation of this reaction. The steady-state catalytic tests identified four classes of materials comprising (i) poorly active (<8%) Fe/SiO_2, Co/SiO_2, Cu/SiO_2, and Ag/SiO_2; (ii) Rh/SiO_2 and Ni/SiO_2, which exhibit intermediate CH_3Br selectivity (<60%); (iii) Ir/SiO_2 and Pt/SiO_2, which display great propensity to CH_4 (>50%); and (iv) Ru/SiO_2, which exhibits the highest selectivity to CH_3Br (up to 96%). In-depth characterization of representative catalysts in fresh and used forms was done by X-ray diffraction, inductively coupled plasma optical emission spectroscopy, N_2 sorption, temperature-programmed reduction, Raman spectroscopy, electron microscopy, and X-ray photoelectron spectroscopy. The dimensionality reduction performed on the 272 DFT intermediate adsorption energies using principal component analysis identified two descriptors that, when employed together with the experimental data in a random forest regressor, enabled the understanding of activity and selectivity trends by connecting them to the energy intervals of the descriptors. In addition, a representative analytic model was found using the Bayesian inference. These findings illustrate the exciting opportunities presented by integrated experimental/computational screening and set the fundamental basis for the accelerated discovery of superior hydrodebromination catalysts and beyond.

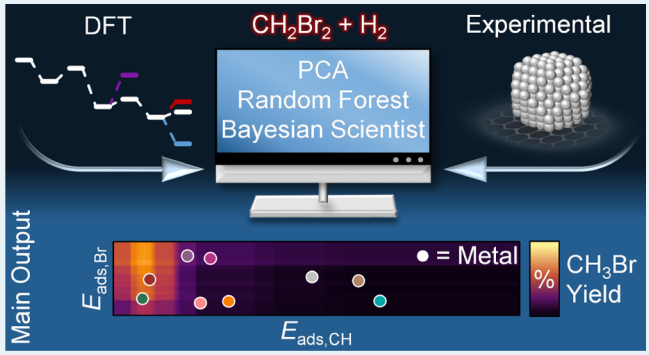

KEYWORDS: *methane activation, dibromomethane, hydrodebromination, principal component analysis, random forest classifier, statistical analysis, density functional theory*

1. INTRODUCTION

The development of innovative approaches enabling the efficient and economical on-site valorization of natural gas into fuels and chemicals has become a strategic research area.[1−4] Among the various technologies, halogen-mediated processes have emerged as viable routes for the transformation of methane, the main constituent of natural gas, into transportable liquids.[5,6] In this regard, bromine is the preferred halogen over chlorine as it provides higher selectivities to the desired bromomethane (CH_3Br).[7,8] In addition, the weaker C−Br bond (2.95 eV) compared to the C−Cl bond (3.51 eV) allows facile HBr elimination, vital for halogen recycling within the process.[9] Nonetheless, the formation of significant amounts of dibromomethane (CH_2Br_2, selectivity up to 32%) in the gas-phase bromination of CH_4 hinders this technology to prosper at industrial scale.[10] Polyhalogenated byproducts shorten the lifetime of zeolites, main catalytic systems for the downstream halomethane coupling step, due to the increased coke formation.[11] The elimination of CH_2Br_2 by CH_4 bromination over heterogeneous catalysts has a limited scope, since the noncatalytic gas-phase radical pathways cannot be fully suppressed,[12] while reproportionation of CH_2Br_2 with CH_4 into CH_3Br requires long residence times (up to 60 s) and is thermodynamically constrained.[13]

In contrast, the selective reforming of polyhalomethanes *via* catalytic hydrodehalogenation, a class of semihydrogenation reactions, presents a practicable approach.[14,15] This reaction

has mainly been studied by Ding *et al.*, reporting the performance of noble-metal-based catalysts (Ru, Rh, Pd, Ag, Pt, and Au) supported on silica.[15] Therein, Pd/SiO_2 was shown to produce oligomers, revealing its full transformation into Pd_6C/SiO_2 under reaction conditions. Selective CH_2Br_2 hydrodebromination to CH_3Br was reported over Ru/SiO_2 (<96% selectivity) and Rh/SiO_2 (<83% selectivity), whereas Pt/SiO_2 produced mainly CH_4 (>47% selectivity to CH_4). Ag was found to rapidly oxidize to AgBr under reaction conditions, whereas Au was inactive. Still, the amount of literature on hydrodebromination chemistry on catalytic surfaces is very limited. In particular, other known hydrogenation catalysts such as Fe, Co, Ni, Cu, and Ir were never studied in this reaction and the stability performance of systems that selectively hydrodebrominate CH_2Br_2 to CH_3Br is not reported.[16,17]

The search for new catalysts typically starts with high-throughput experimental screening and by property similarity within the periodic table. New techniques based on statistical learning (SL) have been tentatively applied to guide this quest.[18] Some degree of success has been achieved when activity and, to a lesser extent, selectivity were taken as response functions.[19−27] The variables introduced as potential descriptors often correspond to preparation variables, for instance, the catalytic composition for optimization of dopant concentrations *via* artificial neural networks.[22−27] The main issues preventing the extensive application of such strategies are the lack of consistency between the databases originating from previous works and the fact that open literature contains only successful experiments, whereas SL techniques require the full scenario (*i.e.*, including conclusive but unsuccessful results) to make robust predictions. Activity descriptors have been reported from linear-scaling relationships (LSRs);[28] however, the identification of these descriptors can benefit SL techniques.

In this work, we present a systematic catalytic preparation and testing protocol coupled to mechanistic studies based on density functional theory (DFT) that can be employed as a complete database for the use of statistical learning inference of trends for a highly active and selective CH_2Br_2 hydrodebromination catalyst. Herein, the toolbox of statistical learning methodologies applied contains dimensionality reduction *via* principal component (PC) analysis (PCA) clustering, and classification techniques.[29−31] The findings reported in this work are first attempts directed at elucidating hydrodebromination performance patterns to lay the foundations for future catalyst design and to pave the way for the wider application of machine learning techniques to, for instance, multimetallic systems.

2. MATERIALS AND METHODS

2.1. Catalyst Preparation. Commercial SiO_2 (Evonik, AEROPERL 300/30, S_{BET} = 257 $m^2\ g^{-1}$, V_{pore} = 0.95 $cm^3\ g^{-1}$, >99.0%) was calcined at 973 K for 5 h in static air (heating rate 5 K min^{-1}) prior to its use as a support in the synthesis protocol. The metal precursors, $Fe(NO_3)_3{\cdot}9H_2O$ (Acros Organics, 99%), $Co(NO_3)_2{\cdot}6NH_3$ (abcr, 99%), $Ni(NO_3)_2{\cdot}6H_2O$ (Strem Chemicals, 99.9%), $Cu(NO_3)_2{\cdot}xH_2O$ (Sigma-Aldrich, 99.999%), $RhCl_3{\cdot}H_2O$ (Acros Organics, 99%), $AgNO_3$ (Sigma-Aldrich, 99.8%), $IrCl_4{\cdot}xH_2O$ (abcr, 99.9%), $RuCl_3{\cdot}xH_2O$ (abcr, 99.9%), and $Pt(NH_3)_4Cl_2{\cdot}xH_2O$ (Sigma-Aldrich, 99%), were dispersed on the support *via* incipient wetness impregnation. Appropriate amounts of the precursors required to obtain a metal loading of 1 wt % in the final catalyst were dissolved in a volume of deionized water equal to the pore volume of the carrier. The precursor solution was added dropwise to the support, and the mixture was magnetically stirred (500 rpm) for 30 min at room temperature. The resulting solids were dried at 373 K for 12 h and calcined in static air at 623 K (heating rate 5 K min^{-1}) to obtain the SiO_2-supported metal oxides, followed by their reduction under 20 vol % H_2 (PanGas, purity 5.0) in He (PanGas, purity 5.0) flow at elevated temperatures (573−968 K) for 3 h in the catalytic reactor with a heating rate of 10 K min^{-1} prior to their use in catalytic tests. The catalysts were referred to as M/SiO_2, where M denotes the metal (*i.e.*, Fe, Co, Ni, Cu, Ru, Rh, Ag, Ir, or Pt). The specific catalyst obtained by direct reduction was denoted M/SiO_2-NC, where NC stands for "noncalcined."

2.2. Catalyst Characterization. Powder X-ray diffraction (XRD) was carried out in a PANalytical X'Pert PRO-MPD diffractometer with Bragg−Brentano geometry by applying Ni-filtered Cu Kα radiation (λ = 1.54060 Å). The data were recorded in the 10−70° 2θ range with an angular step size of 0.017° and a counting time of 0.51 s per step. The metal loading in the solids was determined by inductively coupled plasma optical emission spectroscopy (ICP-OES) using a Horiba Ultima 2 instrument equipped with photomultiplier tube detection. N_2 sorption at 77 K was measured in a Micromeritics TriStar II analyzer. Samples (*ca.* 0.1 g) were degassed to 50 mbar at 573 K for 12 h prior to the measurement. The Brunauer−Emmett−Teller (BET) method was applied to calculate the total surface area, S_{BET}. The pore volume, V_{pore}, was determined from the amount of N_2 adsorbed at a relative pressure of p/p_0 = 0.98. Temperature-programmed reduction with hydrogen (H_2-TPR) was conducted in a Micromeritics AutoChem II 2920 unit equipped with a thermal conductivity detector. The sample (*ca.* 0.1 g) was loaded in a U-shaped quartz reactor between two plugs of quartz wool and pretreated in He (20 $cm^3\ min^{-1}$) at 473 K for 10 min. The analysis was performed in 5 vol % H_2 in N_2 (20 $cm^3\ min^{-1}$) by heating up the catalyst in the range of 323−1100 K at 10 K min^{-1}. Raman spectroscopy was carried out on a WITec CRM200 confocal system using a 532 nm laser with 20 mW power, a 100× objective lens with numerical aperture (NA) = 0.9 (Nikon Plan), and a fiber-coupled grating spectrometer (2400 lines mm^{-1}), giving a spectral sampling resolution of 0.7 cm^{-1}. High-angle annular dark-field scanning transmission electron microscopy (HAADF-STEM) was conducted on an aberration-corrected HD2700CS microscope (Hitachi) at 200 kV. All samples were dispersed in ethanol, and some droplets were deposited onto lacey carbon-coated copper grids. The particle size distribution of the catalysts was obtained by examining more than 100 nanoparticles. X-ray photoelectron spectroscopy (XPS) measurements were performed on a Physical Electronics Quantum 2000 X-ray photoelectron spectrometer using monochromatic Al Kα radiation, generated from an electron beam operated at 15 kV, and equipped with a hemispherical capacitor electron-energy analyzer. The solids were analyzed at an electron takeoff angle of 45° and a pass energy of 46.95 eV. The samples were mounted onto the sample holder by pressing the powders onto an aluminum foil. The spectrometer was calibrated for the 4 Au $4f_{7/2}$ signal to be at 84.0 ± 0.1 eV with a resolution step width of 0.2 eV. The envelopes were fitted by mixed Gaussian−Lorentzian component profiles after Shirley background subtraction. The selected peak positions of the

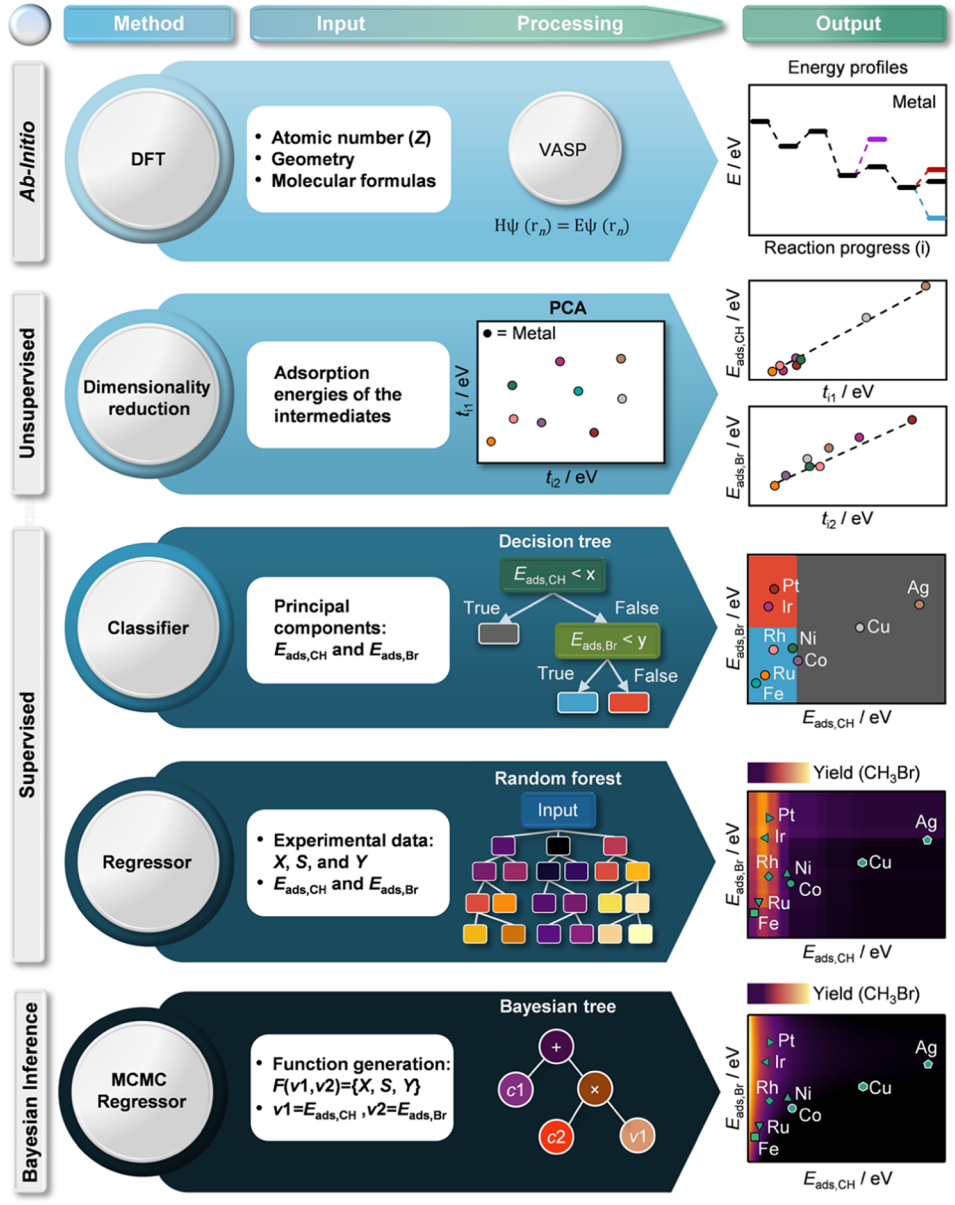

Figure 1. Overview of the multitechnique strategy combining experimentally obtained data, DFT results, and statistical tools to analyze the activity and selectivity of metal-catalyzed CH_2Br_2 hydrodebromination.

different species are based on literature-reported data and fixed with an error of ±0.3 eV.

2.3. Catalyst Testing. The hydrodebromination of dibromomethane was performed at ambient pressure in a home-made continuous-flow fixed-bed reactor setup. H_2 (PanGas, purity 5.0), He (Carrier gas, PanGas, purity 5.0), and Ar (internal standard, PanGas, purity 5.0) were dosed by a set of digital mass flow controllers (Bronkhorst), and liquid CH_2Br_2 (Acros Organics, 99%) was supplied by a syringe pump (Fusion 100, Chemyx) equipped with a water-cooled syringe to a vaporizer unit operated at 393 K. The quartz reactor (internal diameter, d_i = 12 mm) containing the reduced catalyst (catalyst weight, W_{cat} = 0.1−1 g, particle size, d_p = 0.4−0.6 mm) was heated to the desired temperature (T = 423−623 K) in an electric oven under He flow. The catalyst bed was allowed to stabilize for at least 10 min at the desired temperature before the reaction mixture was fed at a total volumetric flow (F_T) of 20−150 cm^3 STP min^{-1} and the desired feed composition of $CH_2Br_2/H_2/Ar/He$ = 6:24:4.5:65.5 (mol %), unless otherwise stated. Downstream linings were heated at 393 K to prevent the condensation of unconverted reactants and/or products. Carbon-containing compounds (CH_2Br_2, CH_3Br, and CH_4) and Ar were quantified online *via* a gas chromatograph equipped with a GS-Carbon PLOT column coupled to a mass spectrometer (GC−MS, Agilent GC 6890, Agilent MSD 5973N). The effluent gas stream was then passed through two impinging bottles in series, containing a 1 M NaOH aqueous solution, for neutralization prior to its release in the ventilation system. After the catalytic tests, the reactor was quenched to room temperature in He flow, and the catalyst was retrieved for characterization studies.

The conversion of dibromomethane in CH_2Br_2 hydrodebromination, $X(CH_2Br_2)$, was calculated using eq 1

$$X(CH_2Br_2) = \frac{n(CH_2Br_2)_{in} - n(CH_2Br_2)_{out}}{n(CH_2Br_2)_{in}} \times 100, \ \%$$ (1)

where $n(CH_2Br_2)_{in}$ and $n(CH_2Br_2)_{out}$ are the molar flows of the reactant at the reactor inlet and outlet, respectively. The selectivity, $S(j)$, to product j (j: CH_3Br, CH_4) was calculated according to eq 2

$$S(j) = \frac{n(j)_{out}}{n(CH_2Br_2)_{in} - n(CH_2Br_2)_{out}} \times 100, \ \%$$ (2)

where $n(j)_{out}$ is the molar flow of product j at the reactor outlet. The turnover frequency, TOF, and reaction rate based on CH_2Br_2 consumption, r, were calculated using eqs 3 and 4, respectively

$$\mathrm{TOF} = \frac{n(CH_2Br_2)_{in} \times X(CH_2Br_2)}{W_{cat} \times \omega_M \times D_M}, \ h^{-1}$$ (3)

$$r = \frac{n(CH_2Br_2)_{in} \times X(CH_2Br_2)}{W_{cat}}, \ mol_{CH_2Br_2}\, s^{-1}\, g_{cat}^{-1}$$ (4)

where ω_M is the metal loading determined by ICP-OES and D_M is the metallic dispersion and is expressed as

$$D_M = \frac{6 \times \phi_M}{\bar{d} \times \sigma_M}$$ (5)

where the area occupied by one surface metal atom is σ_M and the volume occupied by an atom in the metallic state is ϕ_M. The error of the carbon balance, ε_C, used to specify the selectivity to coke, was determined using eq 6

$$\varepsilon_C = \frac{n(CH_2Br_2)_{in} - n(CH_2Br_2)_{out} - n(j)_{out}}{n(CH_2Br_2)_{in}} \times 100, \ \%$$ (6)

Evaluation of the dimensionless moduli based on the criteria of Carberry, Mears, and Weisz–Prater[32,33] indicated that the catalytic tests were performed in the absence of mass and heat transfer limitations. In addition, CH_2Br_2 hydrodebromination tests over selected catalysts performed at variable flow rates and constant F_T/W_{cat} as well as using catalyst particles of different sizes at constant F_T/W_{cat} verified the absence of extra- and intraparticle mass-transfer limitations (Figure S1), respectively.

2.4. Density Functional Theory. Density functional theory on slab models representing the different metals was employed as implemented in the Vienna Ab initio Simulation Package (VASP 5.4.4).[34,35] Generalized gradient approximation with the Perdew–Burke–Ernzerhof (GGA-PBE) functional was used to obtain the exchange–correlation energies.[36] Projector-augmented wave (PAW) method was chosen to represent the inner electrons, and the valence monoelectronic states were represented by plane waves with a cutoff energy of 450 eV. The Γ-centered k-point mesh was generated through the Monkhorst–Pack method.[37−39] Van der Waals interactions were described *via* the Grimme's DFT-D2 with the reparametrized C_6 values for metals by our group.[40,41] Gas-phase molecules were optimized in a box of 15 × 15 × 15 Å^3. The optimized bulk lattice parameters were 2.9175 Å for Ag, 2.5009 Å (c/a 1.6052) for Co, 2.5609 Å for Cu, 2.8317 Å for Fe, 2.7146 Å for Ir, 2.4752 Å for Ni, 2.7959 Å for Pt, 2.6997 Å for Rh, and 2.7058 Å (c/a 1.5824) for Ru. All metals were modeled by a four-layer $p(3 \times 3)$-(111) face-centered cubic (fcc) slab, with the exception of using a four-layer $p(3 \times 3)$-(110) for Fe and a $p(3 \times 3)$-(0001) for Co and Ru. The top two layers were allowed to relax, while the bottom two were fixed to the bulk lattice in all slabs, which were interspaced along the z-direction by a vacuum space of 15 Å, and the arising dipole was corrected.[42] The thresholds were 10^{-5} eV and 0.03 eV Å^{-1} for electronic and ionic relaxations, respectively. Climbing image nudged elastic band (CI-NEB) method,[43,44] improved dimer method,[45,46] and quasi-Newton algorithms were employed to locate the transition states (TSs) in the reaction profiles, where the TSs were further verified by their single imaginary frequency character.[45] This data constitutes the first step of our computational analysis as shown in Figure 1. All of the structures have been uploaded to the ioChem-BD database.[47−49]

2.5. Statistical Learning Toolbox. Two main techniques, principal component analysis (PCA) and random forest (RF) regressor,[50,51] have been employed in the statistical treatment of the experimental data and DFT results (Figure 1). One of the major issues of DFT simulations for complex reaction networks is the large number of elementary steps (Figure 1, first row) and that reaction profiles cannot be directly used to map activity and selectivity. Descriptors have been traditionally found by a combination of linear-scaling relationships (LSRs, linking the thermodynamics of adsorption of some intermediates to others) and heuristics based on simple chemical concepts (number of bonds and valences).[52] However, this choice is somewhat nonunivocal as it is not based on a rigorous mathematic algorithm (for instance, it does not ensure orthogonality of the different descriptors).[53] This explains why there are dependencies in multidimensional descriptors, particularly in metals. Alternatively, statistical learning techniques provide a mathematically sound framework to identify descriptors. Thus, the dimensionality reduction of the adsorption energies of all of the intermediates involved in the CH_2Br_2 reaction was done *via* an unsupervised statistical learning method to retrieve the principal components from the data set containing 272 DFT-computed intermediate adsorption energies (Figure 1, second row).[29] The outcomes of the analysis are the principal components (linearly uncorrelated variables), in our case, two different energy terms. Thus, the procedure maps the mathematical descriptors to two energies that represent the covalent and redox contributions. More importantly, PCA allows us to cleanse the data to avoid dependencies and therefore focuses the search between the catalytic response and the descriptors.

The next step constitutes the catalytic performance analysis. Ideally, a full microkinetic model based on the DFT-computed parameters would be the response function to be fitted by the descriptors that were identified *via* the principal components. However, the accuracy and robustness of these methodologies prevent us from performing a full *in silico* analysis.[54] Therefore, the experiments are taken as input and understood with the descriptors obtained computationally. The simplest approach would be to utilize a classifier employing, for instance, K-means, which is popular in data mining, or clustering techniques. However, these methods fail when applied to understand selectivity problems since very small variations in the energy scale of intermediates can lead to a complete switch of the selectivity.[28,29] Alternatively, a simple classifier such as the decision tree (DT) can be employed by answering a list of simple energy-related questions for the two descriptors (vide

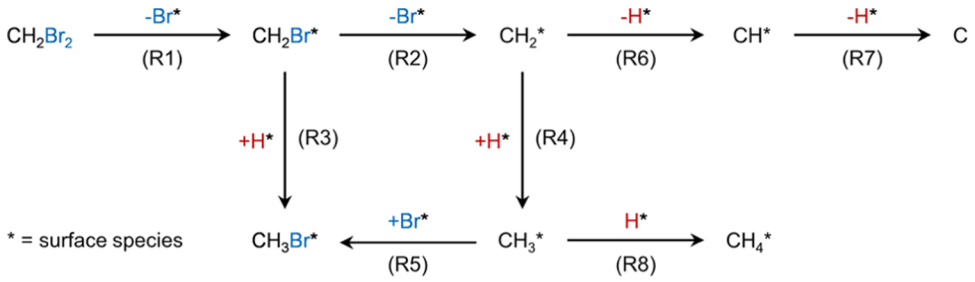

Figure 2. Reaction network of CH_2Br_2 hydrodebromination showing the pathways leading to CH_3Br, CH_4, and C that accounts for coke formation. Arrow labels indicate species involved in the reaction, while the labels in parentheses indicate thermodynamic and kinetic parameters that are detailed in Tables S1−S7.

infra) as shown in the third step in Figure 1. However, these models tend to overfit and alternatives have been proposed in the literature to mitigate this drawback.[50] Therefore, we opted for an ensemble learning method that allows simultaneous classification and regression, thereby overcoming the previously mentioned issues (Figure 1, bottom row). The RF[51] technique operates by constructing an ensemble of decision trees with different seeds, thereby limiting overfitting. Hereafter, the average of the forest is taken as the outcome of the statistical analysis, although a few disclaimers are needed. Typically, random forests are applied to larger data sets and are benchmarked *via* cross-validation. Even though the sets derived from nanoparticles of metals of comparable size are limited, the filtering introduced with the PCA ensures that the results are qualitatively sound. Finally, the analytical functions for the experimental activity, selectivity, and yield have been identified through the Bayesian Machine Scientist (BMS).[55] The algorithm searches for candidate functions that describe the behavior of a given data set using the Markov chain Monte Carlo (MCMC) method. At every Monte Carlo step, the algorithm evaluates the quality of the current function using a complexity parameter, based on the entanglement of the mathematical operators, and an error parameter that depends on the sum of the square estimate of the errors (SSEs). Filtering these values makes it is possible to obtain simple and accurate equations that properly describe the nature of the data set. In our case, the data set contains both the experimental results of activity, selectivity, and yield and the PCA that provides the descriptors from the DFT part. Expansion of the data to variable nanoparticle sizes, speciation, alloys, and intermetallics is beyond the scope of this study but would constitute a natural extension to this work.

3. RESULTS AND DISCUSSION

The state-of-the-art catalytic research work normally encompasses the experimental testing of a few materials, typically reporting only the best hits in terms of activity and selectivity and the study of the reaction network presenting the list of elementary steps and the reaction profiles provided by DFT. Advanced methodologies would include the use of LSR to make a dimensionality reduction that provides one or two descriptors (in some cases, the selection is nonunivocal). A kinetic model based on the particular mechanism found for a single catalyst (typically, a metal) is then simplified *via* a rate-determining-step concept while considering the experimental conditions. Applying the LSR, the rate is simplified to be a function of a single descriptor parameter, leading to what are known as volcano plots.[28] Screening for different materials is then done by computing energies of the descriptor over a family of materials. However, this approach presents a few pitfalls: (i) the selection of the descriptor is nonunivocal; (ii) the probability that there are hidden dependencies is high when there is more than one descriptor; as a consequence, multidimensional analysis (considering more than one descriptor) typically ends up with the activity of all metals falling along the same line; (iii) selectivity is difficult to track due to the small energy differences involved in the selectivity switches (cliffs); and (iv) the studies of stability are introduced in a separate step as a filter to the overall results.

In this work, we have taken an alternative route to combine both experimental and theoretical results to avoid some of these bottlenecks by the generation of an extensive database of catalytic materials, using their activity and selectivity, and employing DFT data as an independent source for the performance descriptors through the inference *via* statistical learning techniques. To this end, the dimensionality reduction of the energies for intermediates is performed *via* a PCA and the random tree and random forest methodologies are employed as a classifier and regressor, respectively, to understand and determine the key binding energies (BEs) for the descriptors that limit the areas with higher activity and selectivity. Formulae for the different response functions, activity, selectivity, and yield, are found using the Bayesian machine scientist employing the computed descriptors.

3.1. Mechanistic Studies and Dimensionality Reduction. The DFT calculations revealed the reaction profiles of CH_2Br_2 hydrodebromination over the nine metals (Fe, Co, Ni, Cu, Ru, Rh, Ag, Ir, and Pt; see Figure S2). The energies for the kinetic and thermodynamic parameters of the reactions shown in Figure 2 are presented in Tables S1−S7 and in the ioChem-BD database, where they can be downloaded as a csv file.[48,49] Three main reasons led to the use of pure metal surfaces as a starting point in the reactivity studies: (i) they allow a systematic investigation while keeping the nature of the materials constant (and thus equivalent electronic structures); (ii) they can provide the fundamentals for the phase transition during the induction process and explain the sources of catalyst instability simultaneously; and (iii) they constitute the simplest type of DFT calculations. The starting point for obtaining the reaction profiles over all nine metals was the mapping of the full path over the Ru surface (Figure 3). The potential transition-state structures on the other metal surfaces (Figure S2) were inherited from that of Ru by applying a previously reported algorithm that uses the potential seed TSs as input for an improved dimer method or a CI-NEB refinement, after which the final structure is confirmed through vibrational analysis.[56] This procedure allowed us to reduce the computational time as the intermediates along the reaction do not

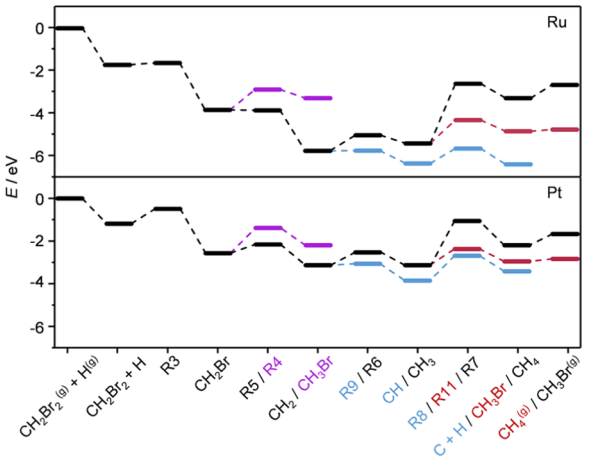

Figure 3. Energy profiles of CH_2Br_2 hydrodebromination on ruthenium and platinum surfaces.

require large optimizations and even the transition states could be directly located from the Ru seed.

The reaction profiles show the sequential elimination of either Br and H atoms and the recombination of the carbonaceous fragments with the main products (CH_4 and CH_3Br) and surface coke illustrated by a carbon precursor. This sequential mechanism exists in all cases except for Fe (Figure S2), on which the CH_2Br intermediate cannot be located. The large reactivity of Fe with respect to the reactants is responsible for the direct decomposition of CH_2Br_2, losing its both Br atoms on the surface. To identify the activity descriptors, a PCA was performed by taking all of the 272 intermediate energies of CH_xBr_y and the isolated atoms H, C, and Br. For all species, several potential adsorption sites were investigated.[29] In the case of CH_2Br_2, physisorption and dissociative adsorption of the C−Br bond occurs on the metal surface. Ultimately, the values of the principal components are 92.8, 5.2, and 1.2%. Therefore, two principal components account for 98% of the adsorption energies and are thus taken as relevant. Then, to unravel the descriptors, we adopted the strategy of mapping these principal component terms to the energies of some of the smallest fragments in the reaction network. We have followed the same mathematical procedure as in our previous work,[29] where the energies of the fragments are correlated with the PC taking the ones showing the lowest error in the prediction. In a second step, we map the PC to the intermediate energies that are better represented by a single PC. When doing so, the first and second PCs were determined as the CH and Br species on the hcp sites, whereas their adsorption energies were considered the descriptors for the covalent (CH) and redox (Br) terms (Figures S3 and S4), respectively, due to their exclusive contribution to these principal components. The role of coverage effects on these parameters for the most active catalyst is shown in Figure S5.

3.2. Catalytic Performance in CH_2Br_2 Hydrodebromination. Gas-phase CH_2Br_2 hydrodebromination was investigated over Fe-, Co-, Ni-, Cu-, Ru-, Rh-, Ag-, Ir-, and Pt-based catalysts supported on SiO_2 (1.0 wt % metal basis), which were chosen based on previously reported CH_2Br_2 hydrogenation studies.[15] The inertness of SiO_2 in hydrodehalogenation reactions and its minimal interaction with the active phase allow studying the intrinsic catalytic performance of each transition metal. Synthesis of the catalysts was done by incipient wetness impregnation, involving a calcination step in air followed by reduction in H_2 prior to their exposure to reaction conditions. The reduction temperature was based on H_2-TPR analysis and was chosen as such to ensure the formation of the metallic phase (Figure S6). Characterization data of the catalysts revealed the close similarity of the specific surface areas (S_{BET}, 244−258 $m^2\ g^{-1}$) and pore volumes (V_{pore}, 0.71−0.83 $cm^3\ g^{-1}$) (Table 1). XRD analysis of the catalysts

Table 1. Characterization Data of the Catalysts

		S_{BET}[b] ($m^2\ g^{-1}$)		V_{pore}[c] ($cm^3\ g^{-1}$)	
catalyst	metal loading[a] (wt %)	fresh	1 h (10 h)	fresh	1 h (10 h)
Fe/SiO_2	1.1	254	254	0.77	0.76
Co/SiO_2	0.9	258	250	0.79	0.78
Ni/SiO_2	1.0	254	252 (240)	0.75	0.80 (0.71)
Ni/SiO_2-NC	1.0	251	244	0.77	0.79
Cu/SiO_2	0.9	255	251	0.78	0.77
Ru/SiO_2	1.0	247	254 (246)	0.71	0.73 (0.70)
Ru/SiO_2-NC	1.0	249	240	0.83	0.80
Rh/SiO_2	1.0	250	220 (228)	0.77	0.72 (0.70)
Ag/SiO_2	0.9	250	249	0.76	0.72
Ir/SiO_2	1.0	254	253 (246)	0.76	0.73 (0.72)
Pt/SiO_2	1.0	244	242 (245)	0.77	0.75 (0.73)

[a]ICP-OES. [b]BET model. [c]Volume of N_2 adsorbed at $p/p_0 = 0.98$.

showed diffraction peaks compatible with the metallic phases, whereas no evidence of the oxide phases was observed (Figure 4a). Further confirmation of the elemental composition was provided by ICP-OES, which showed that the metal content in the materials was approximately the targeted 1.0 wt %. The structural information gained from the utilization of XRD was corroborated by Raman spectroscopy (Figure 4b). All catalysts displayed low-frequency bands centered at 490 and 603 cm^{-1}, which are characteristic of the SiO_2 support.[57,58] In addition, the Raman spectrum of Ir/SiO_2 evidenced bands at 548 and 716 cm^{-1}, which could be ascribed to a minor IrO_2 phase,[59,60] and the spectrum of Cu/SiO_2 displayed a band at 972 cm^{-1}, suggesting that a Cu_xSiO_y phase is likely present in the respective supported Ir and Cu catalysts.[61,62] The presence of Cu_xSiO_y could explain the reduction peak at *ca.* 500 K observed in H_2-TPR (Figure S6).[62]

The catalysts were evaluated in CH_2Br_2 hydrodebromination at different reaction temperatures (423−623 K). Assessment of the hydrodebromination activity, expressed as CH_2Br_2 conversion, at 523 K allowed derivation of the following order for the respective supported catalyst: Fe ≈ Co ≈ Cu ≈ Ag (4−7%) < Ni (11%) < Ru (19%) < Rh (32%) < Ir ≈ Pt (50−52%) (Figures 5a and S7). Evaluation of the product selectivities at 523 K and *ca.* 20% CH_2Br_2 conversion achieved by adjustment of the space velocity is shown in Figure 5b. The performance of Fe, Co, Cu, and Ag showed consistency with the generally reported inferior hydrogenation activity of these elements compared to the platinum group metals. From a cost perspective, it is interesting that Ni displays a selectivity pattern comparable to that of Rh.

3.3. Classification of Metal Catalysts Using the Random Forest Regressor. Four clusters are classified based on the experimentally determined product distribution of the SiO_2-supported metal catalysts: (i) poor hydrodebromination activity over Fe, Co, Cu, and Ag, with coke

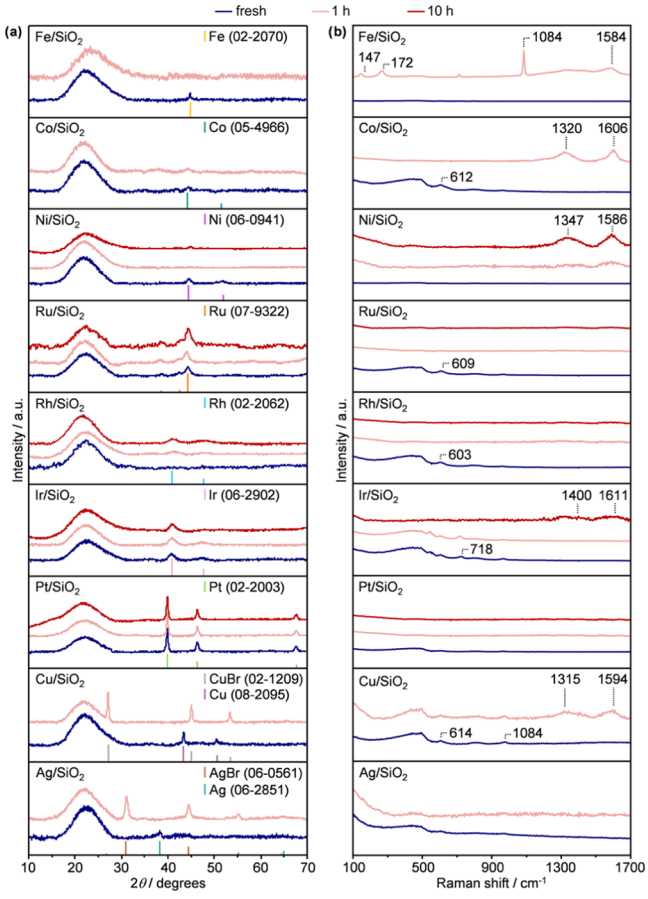

Figure 4. (a) XRD patterns and (b) Raman spectra of the catalysts in a fresh form and after CH_2Br_2 hydrodebromination. Reference diffraction patterns are shown as vertical lines below the measured diffractograms and are identified with their ICDD-PDF numbers. Reaction conditions: $CH_2Br_2/H_2/Ar/He$ = 6:24:4.5:65.5, F_T/W_{cat} = 25−150 $cm^3\ min^{-1}\ g_{cat}^{-1}$, T = 523 K, P = 1 bar, and time on stream (tos) = 1 or 10 h.

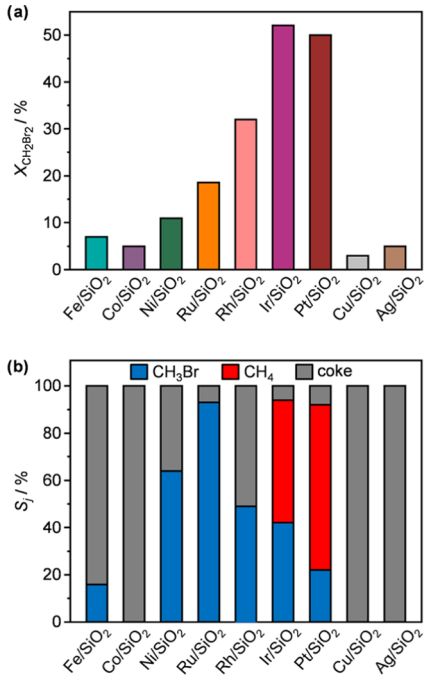

Figure 5. (a) Conversion of CH_2Br_2 and (b) product selectivity of the catalysts in CH_2Br_2 hydrodebromination. In (a), the conversion was assessed at a constant space velocity of F_T/W_{cat} = 40 $cm^3\ min^{-1}\ g_{cat}^{-1}$, while product selectivities in (b) were determined at *ca.* 20% CH_2Br_2 conversion achieved by adjusting the space velocity in the range of F_T/W_{cat} = 20−150 $cm^3\ min^{-1}\ g_{cat}^{-1}$. Other reaction conditions: $CH_2Br_2/H_2/Ar/He$ = 6:24:4.5:65.5, T = 523 K, P = 1 bar, and tos = 0.25 h.

as the main product. (ii) Intermediate activity and selectivity to CH_3Br (<55 and <58%, respectively) over Ni and Rh, coupled with pronounced coke formation. Worth mentioning is the absence of CH_4 generation over these two groups of catalysts at any reaction temperature applied (Figure S7). (iii) Great propensity to CH_4 (>48 and >61%, respectively) besides producing CH_3Br (<28 and <39%, respectively) over Ir and Pt with minor coking. (iv) The highest selectivity to CH_3Br (<96%) over Ru with coke (<23%) as the byproduct (notably higher than any other metal). The qualitative analysis of the main product with a single decision tree shows that only two decisions are needed to classify all of the observations (Figure 1): the main decision corresponds to the CH binding energy, while the second is the binding energy of Br, in agreement with the PCA.

Then, experimental performance can be analyzed in terms of the PC through the random forest technique. Therein, the experimentally determined CH_2Br_2 conversion, CH_3Br yield, CH_3Br selectivity, and the two descriptors obtained by PCA were taken as inputs (Figure 1). A random forest algorithm composed of 128 trees was trained to sample the phase space spanned by the descriptors.[50] Tests with different tree lengths and number of trees are presented in the SI (Figure S8). The accuracy of the training set is 0.91 for the conversion, 0.79 for the selectivity, and 0.87 for the yield. This allows the partition of the performance of the different catalysts just by taking the properties of the naked metal surfaces without considering potential phase transformations (Figure 6).

For the highest conversion, the optimal CH adsorption energy ranges from −6.50 to −6.75 eV (with respect to the $CH^{(g)}$ fragment), while the ideal Br adsorption energy requires a weak M−Br bond (Figure S2). This explains the inactive behavior of Co, Cu, and Ag, since they hold either far-too-strong or far-too-weak CH adsorption regions. The selectivity frontiers are different from the activity ones, as previously described for general reactivity models.[28] In particular, selectivity toward CH_3Br requires a weaker CH and stronger Br adsorption energy than the one for activity, with ranges from −6.30 to −6.75 eV and from −2.2 to −2.3 eV, respectively. It should be emphasized that there is a narrow selectivity window for CH_3Br, which spans only 0.1 eV along the Br binding energy direction. Ru, with the best catalytic behavior, is close to the sweet spot, and Ir and Pt are in the weak binding region (Figure 6). Finally, the performance of Fe sets up a new region due to its different packing way that leads to the variations of surface metal positions from the standard fcc metals. As a result, the descriptors correspond to very exothermic energies and the area, likely to be shared with other early transition metals, would correspond to a poorly active region.

3.4. Identification of the Functional Forms for the Catalytic Activity of the Metal Catalysts Using the Bayesian Machine Scientist (BMS). The RF methods present three main drawbacks: (i) their black-box nature masks the physical interpretability of the trained model (a

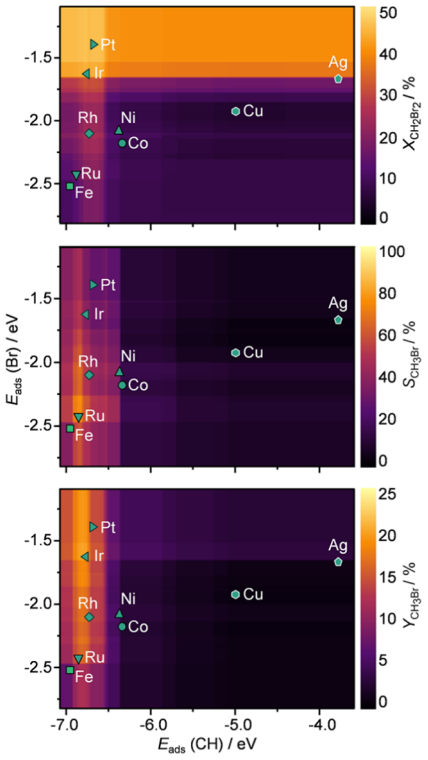

Figure 6. CH_2Br_2 conversion, CH_3Br selectivity, and CH_3Br yield for different values of E_{ads}(CH) and E_{ads}(Br) obtained with a random forest regressor algorithm containing 128 trees.

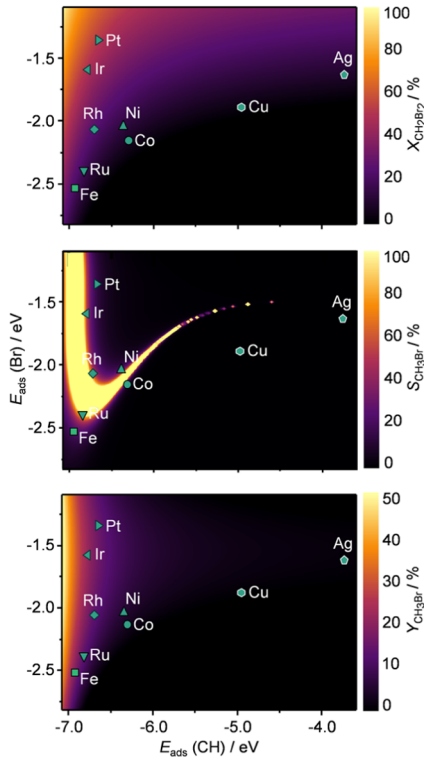

Figure 7. CH_2Br_2 conversion, CH_3Br selectivity, and CH_3Br yield for different values of E_{ads}(CH) and E_{ads}(Br) obtained with the Bayesian machine scientist using the functions: $X = -(E_{ads}(Br_{hcp}) - c_{c_1})\cdot c_{c_2} + \frac{c_{c_3}}{E_{ads}(CH) + c_{c_4}}$ for the conversion, $S = -((E_{ads}(Br) - c_{s_1})\cdot(E_{ads}(CH) + c_{s_3})^{E_{ads}(CH)+c_{s_3}+1} + (E_{ads}(CH) + c_{s_3}) + c_{s_2})^{-2}$ for the selectivity, and $Y = -(E_{ads}(Br) + c_{y_1})^2\cdot c_{y_2} + \frac{c_{y_2}}{(E_{ads}(CH) + c_{y_3})^2}$ for the yield. Fe was not included during the functional form search.

numerical value with an error is retrieved as a response), (ii) the range and accuracy are closely related to the number of samples used in the training phase, and (iii) extracting a functional form is difficult. To overcome these issues, BMS[55] has been employed to search for general functional forms (Figure S9 and Tables S9–S11) that describe the response functions (experimental conversion, selectivity, and yield) for CH_2Br_2 hydrodebromination taking DFT-PCA descriptors as variables. To homogenize our data set, Fe has been excluded from the input data set due to its different atom packing.

Figure 7 shows the best functions obtained for each experimental parameter and their graphical representation. Conversion has the simplest equation, displaying a direct dependence on the adsorption energy of Br and an inverse dependence on the adsorption energy of CH. These dependencies point to a possible surface Br contamination in metals with the most exothermic Br–metal bonds. Contrarily, conversion improves at lower values of CH adsorption energy. Significantly, the equation for the yield is the squared of the conversion. Therefore, it describes a volcano-like area with the highest response values at the most exothermic CH adsorption and intermediate values of Br adsorption energies. Finally, the function obtained to represent the selectivity is rather complex and hard to interpret. However, its graphic representation shows a cliff cutting the area between the metals that coke and those that do not, correctly reproducing the opposite behavior of Co and Ni. Table S12 contains the fitting parameters of the found functions. Additionally, Figure S10 shows an additional simple functional form found for selectivity.

Figure 8 shows the obtained SSE comparing the experimental and predicted values using the two regressors. BMS is the method that achieves the best accuracy for all of the experimental values. However, the dependency of RF on the number of samples and the complexity of the selectivity equation obtained with BMS leads us to think that for rough areas such as selectivity, RF will perform a better prediction with denser samples. Contrarily, BMS can provide simple models with a limited number of observations, as can be seen for conversion and yield. Additional information about prediction errors can be found in Table S8.

3.5. Stability and Characterization of the Used Catalysts. Establishing typical product distributions for each metal naturally raises questions as to how the materials behave upon exposure to reaction conditions for longer times. Therefore, product-based trends identified were complemented with short-term (10 h) CH_2Br_2 hydrodebromination tests over the active SiO_2-supported catalysts (Ni, Rh, Ir, Pt, and Ru), evidencing deactivation of all catalytic systems with *ca.* 25–80% loss of initial activity (Figure S11). The following order of decreasing stability over 10 h was found: Rh ≈ Ru ≈ Ni < Ir ≈ Pt. Therein, Ni falls out of the trends by showing a significant loss of CH_2Br_2 conversion in the first 2 h on stream and displaying relatively stable performance for the remainder of the reaction time. On the other hand, Ru follows a similar deactivation profile as Rh, gradually losing activity over time. A moderate decrease in performance was achieved over Ir and Pt, showing *ca.* 1.5–3.5 times more activity compared to the rest of the metal catalysts. Depletion of activity was appended by moderate changes in the product distribution. With time on

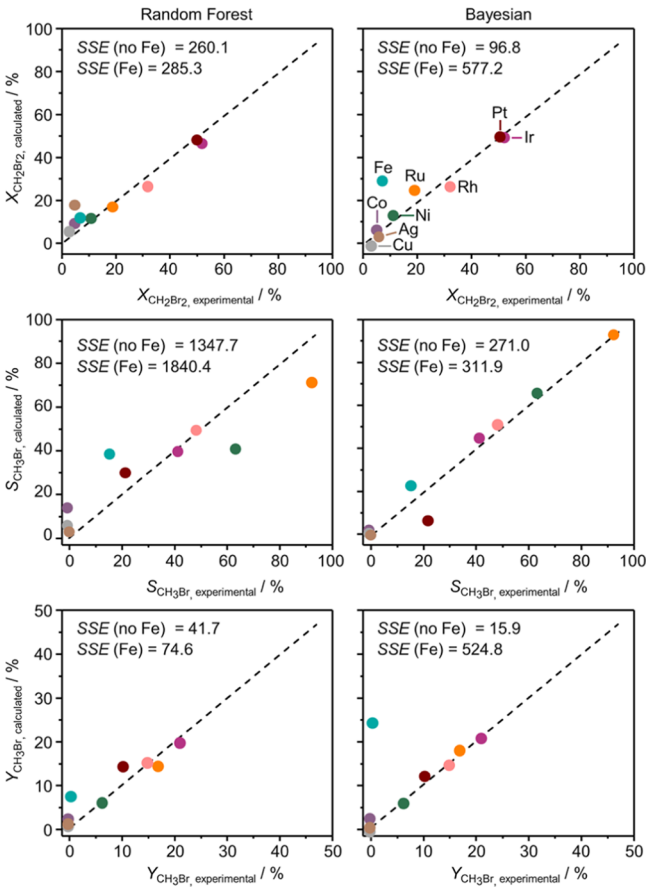

Figure 8. Sum of squared estimate of errors (SSEs) comparing the experimentally obtained CH_2Br_2 conversion, CH_3Br selectivity, and CH_3Br yield with their predicted values using the Bayesian machine scientist and the trained random forest regressor.

stream, the selectivity to CH_3Br progressively decreased over Rh, Ir, and Pt, whereas a slight increase was observed over Ni and Ru. The propensity to form CH_4 was enhanced over Ir and Pt, while changes in coke production were mainly observed over Ni and Rh. These findings emphasize that catalyst robustness remains a challenge, for which understanding the origin of deactivation is essential to develop superior CH_2Br_2 hydrodebromination catalysts.

SiO_2-supported metals that exhibit poor activity (Fe, Co, Cu, and Ag) were characterized after 1 h on stream, whereas analysis of the catalytically active systems (Ni, Ru, Rh, Ir, and Pt) was performed after 1 and 10 h use in CH_2Br_2 hydrodebromination. In particular, N_2-sorption, ICP-OES, XRD, and Raman spectroscopy were applied to study the development of the materials during exposure to the reaction environment. Examination of the textural properties by N_2-sorption showed minimal differences in the specific surface areas (S_{BET}) and pore volumes (V_{pore}) of the used (1 and/or 10 h) and fresh samples (Table 1). Furthermore, quantification of the metal content in used systems by ICP-OES analysis pointed toward the preservation of the metal content (1.0 wt %) in all catalysts, indicating the absence of active phase leaching or volatilization. Further investigation revealed three main deactivation mechanisms: (i) bromination, (ii) fouling by coking, and (iii) active phase restructuring.

Generally, the presence of a halogen introduces structural stability challenges for many catalysts.[63] Analysis of the Ag/SiO_2 and Cu/SiO_2 samples confirmed the severe effects of bromination on activity. In line with the literature, the poor performance of Ag could be explained by its rapid oxidization to AgBr as observed in XRD (Figure 4a).[15] A similar behavior was observed for Cu, which was promptly restructured to CuBr. The XRD reflections of used Co/SiO_2 resembled those of the fresh material, suggesting the absence of active phase sintering or extensive bromination. In contrast, the disappearance of the reflection assigned to metallic iron in Fe/SiO_2 points toward restructuring after exposure to reaction conditions. Complemented with Raman analysis (Figure 4b), the spectra of used Fe/SiO_2 evidenced minor bands at 147 and 272 cm^{-1}, which could be attributed to Fe−Br and Fe−C stretching modes, respectively, with the latter most likely due to the presence of Fe_xC_y phases.[64−67] Moreover, a strong band was detected at 1084 cm^{-1}, which relates to the asymmetric stretching mode of Fe−O−Si bonds in tetrahedrally coordinated Fe species.[68] Altogether, Raman analysis suggests the prompt restructuring of metallic Fe to $FeBr_x$, Fe_xC_y, and FeO_xSi_y under hydrodebromination conditions, rendering the catalyst very complex (in agreement with the difficulties found in the simulations) and mostly inactive. In addition, the Raman spectra of used Fe/SiO_2, Cu/SiO_2, and Ni/SiO_2 display the well-documented D and G bands at *ca.* 1320 and 1585 cm^{-1}, which are ascribed to graphitic species and normal vibrations in graphene, respectively.[69,70] In addition to the D band, Co/SiO_2 and Ir/SiO_2 show a significant peak at *ca.* 1606 cm^{-1}, commonly denoted the D′ band, signifying the presence of imperfect graphite or disordered carbon.[71] This indicates that coke formation, the main deactivation mechanism over Co/SiO_2 and Ir/SiO_2, follows a different pathway compared to Fe and Cu.

In addition to the previously mentioned characterization techniques, XPS and HAADF-STEM microscopy were adopted to further study the catalytically active systems that were exposed to 10 h hydrodebromination conditions (Figure S11). Therein, HAADF-STEM observations disclosed the dispersion of Ni, Ru, Rh, Ir, and Pt nanoparticles on SiO_2. Rh- and Pt-based materials displayed a narrow size distribution, whereas a wide size distribution was found for Ni, Ru, and Ir-based systems (Figure 9). Although the micrographs indicate that Pt/SiO_2 exhibits an average particle size distribution of 2.2 nm, a few particles in the range of 18−28 nm were distinguished, too. Moreover, large Pt crystallites of up to *ca.* 100 nm could be appraised quantitatively from XRD analysis, providing this numerical estimation based on the Scherrer equation (Figure 4a). Compared to their fresh analogues, used Ni-, Ir-, and Pt-based systems showed small changes in the average metal nanoparticle size. In contrast, pronounced active phase sintering in Ru/SiO_2 and Rh/SiO_2 strongly reduced the fraction of surface metal atoms after 10 h on stream by *ca.* 30 and 40%, respectively, demonstrating that this deactivation mechanism occurs on various nanoparticle-based catalysts regardless of the halogen source.[14] The systems were further analyzed by XPS to assess the presence of brominated metal species on the surface of the used materials, revealing that bromination plays a limited role in catalyst deactivation (Figure 10). The Ru 3d, Rh 3d, Ir 4f, and Pt 4f core-level spectra of the fresh and used systems displayed pronounced peaks at binding energies (BEs) of *ca.* 279.1, 306.9, 60.4, and 70.7 eV, respectively, corresponding to the metallic phase.[72−74] Careful fitting of the spectra revealed contributions at BEs of 72.2 and 74.0 eV in Pt/SiO_2, at 61.9 eV in Ir/SiO_2, and at

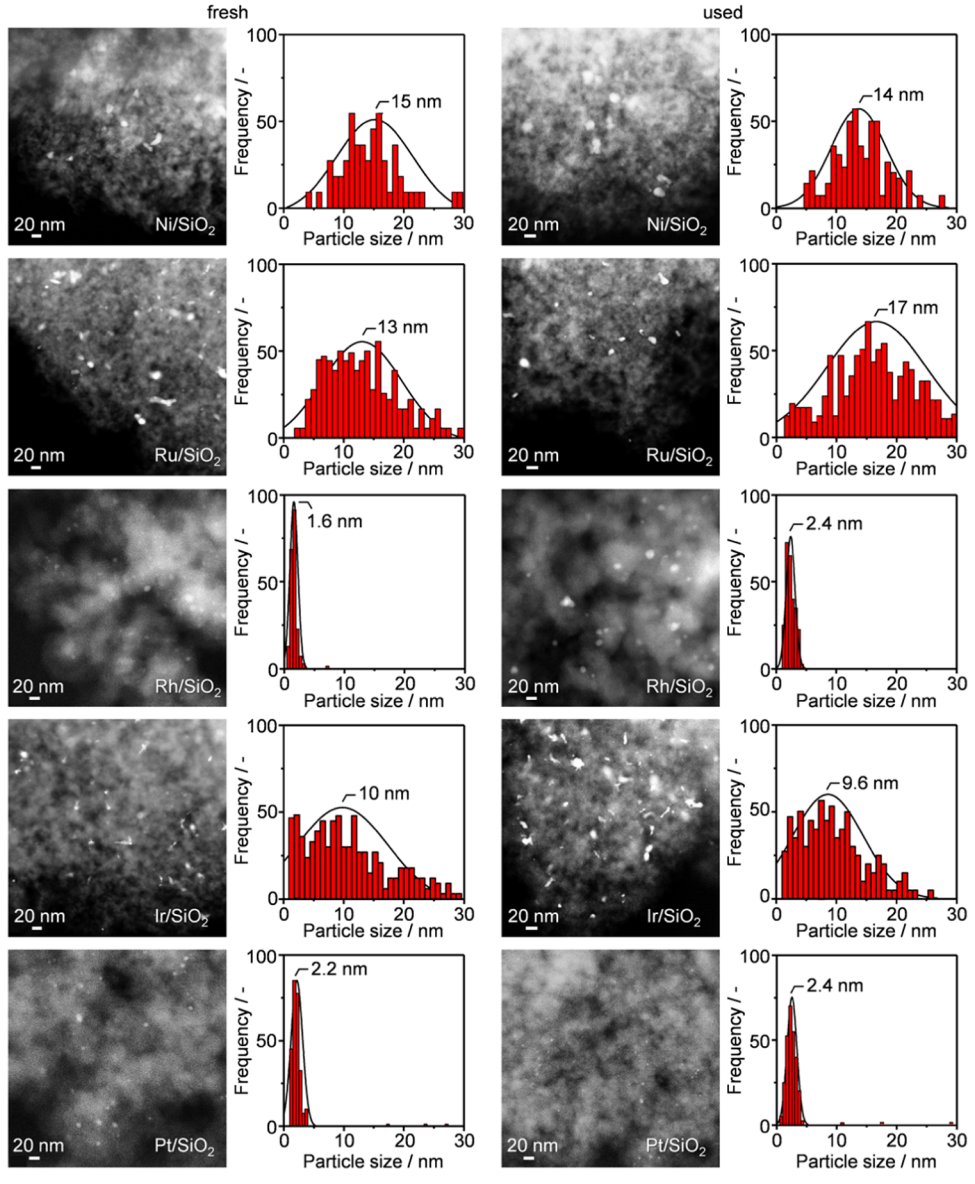

Figure 9. HAADF-STEM micrographs and derived particle size distributions of selected catalysts in a fresh form and after 10 h in CH_2Br_2 hydrodebromination. The conditions specified in Figure 4 apply here.

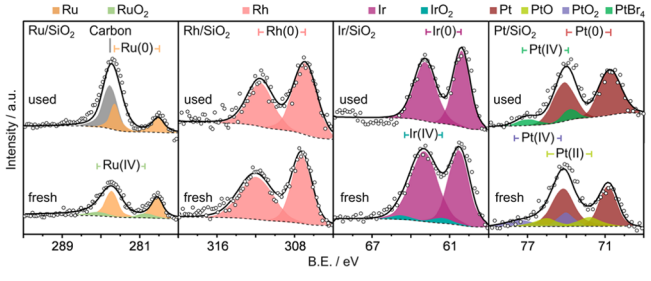

Figure 10. Ru 3d, Rh 3d, Ir 4f, and Pt 4f XPS core-level spectra of selected catalysts in a fresh form and after 10 h in CH_2Br_2 hydrodebromination. The solid lines and the open circles represent the overall fit and the raw data, respectively, while the colored areas beneath them indicate the different contributions. The conditions specified in Figure 4 apply here.

280.6 eV in Ru/SiO_2, all designated to oxidized species,[72,73,75] likely due to exposure of the sample to air. Minor active phase bromination (<15%) was observed over used Pt/SiO_2, as indicated by the peak at a BE of 73.8 eV, which is ascribed to $PtBr_4$ species.[76] The presence of carbon species (*ca.* 30%) was detected over used Ru/SiO_2, as evidenced by the strong contribution at a BE of 284.2 eV. The Ni-based system suffered from the formation of an oxidized Ni layer formed by contact of the sample with air, a process well-studied in literature.[77] Sputtering prior to XPS analysis would remove potential Br species present on the surface, preventing any realistic comparison with other catalysts. The use of operando spectroscopic techniques could provide more insights into the deactivation phenomena. However, the application of such methods requires the design of adequate cells resistant to the corrosive nature of this reaction, which will be the subject of future investigations.

3.6. Kinetic Analysis. To further compare and benchmark the performance of the catalytically active systems, TOF values of selected materials were determined (Figure 11a). Ni/SiO_2, Ru/SiO_2, and Pt/SiO_2 were chosen as representative systems of their respective performance group. The dispersion was

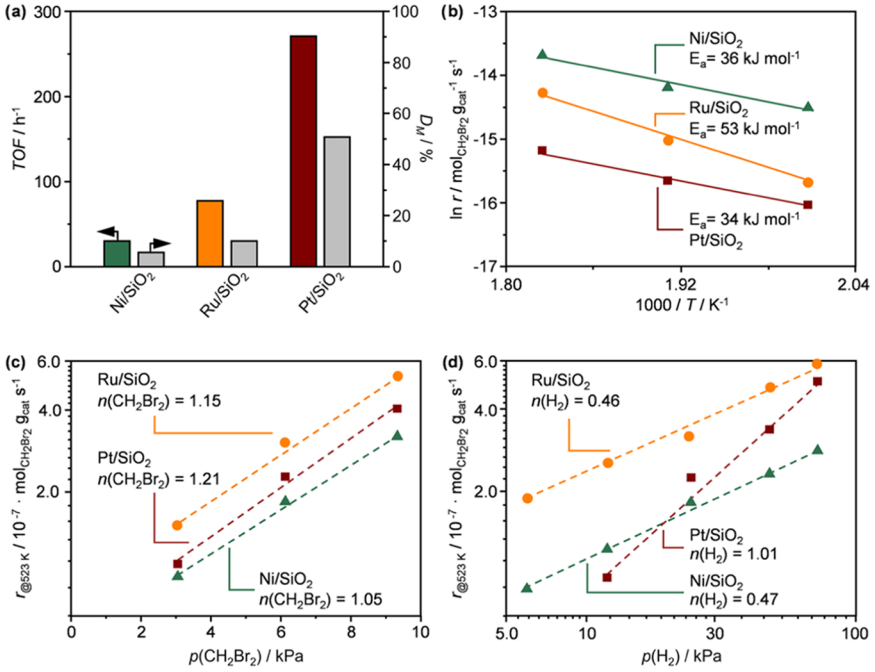

Figure 11. (a) Turnover frequencies and rates of CH_2Br_2 hydrodebromination over selected catalysts as a function of (b) temperature and inlet partial pressures of (c) CH_2Br_2 and (d) H_2. Each catalytic data point was gathered using materials in a fresh form to exclude the possible influence of catalyst deactivation. Reaction conditions: (a) $CH_2Br_2/H_2/Ar/He$ = 6:24:4.5:65.5, F_T/W_{cat} = 40 $cm^3\ min^{-1}\ g_{cat}^{-1}$, and T = 523 K; (b) $CH_2Br_2/H_2/Ar/He$ = 6:24:4.5:65.5, F_T/W_{cat} = 40−200 $cm^3\ min^{-1}\ g_{cat}^{-1}$, and T = 498−548 K; (c) $CH_2Br_2/H_2/Ar/He$ = 3−9:24:4.5:62.5−68.5, F_T/W_{cat} = 40−200 $cm^3\ min^{-1}\ g_{cat}^{-1}$, and T = 523 K; and (d) $CH_2Br_2/H_2/Ar/He$ = 6:6−72:4.5:17.5−83.5, F_T/W_{cat} = 40−200 $cm^3\ min^{-1}\ g_{cat}^{-1}$, and T = 523 K. All tests were conducted at P = 1 bar and tos = 0.25 h.

calculated based on the average metal nanoparticle size, assuming a hemispherical geometry of the metal site as observed in the micrographs (Figure 9). The activity of the catalysts decreased in the following order: $Pt/SiO_2 \gg Ru/SiO_2 > Ni/SiO_2$, with dispersions of 51, 10, and 7%, respectively, confirming the previously determined trends (Figure 5a). As shown in Figure 11a, Pt/SiO_2 displays TOF values *ca.* 1 order of magnitude higher than those observed over the other systems. The dispersion values of Ni/SiO_2 and Ru/SiO_2 differ significantly from that of Pt/SiO_2. To eliminate a possible influence of this parameter, reference catalysts with comparable active phase dispersion were synthesized by omitting the calcination step during the synthesis to obtain Ni/SiO_2-NC and Ru/SiO_2-NC. XRD analysis and HAADF-STEM microscopy confirmed the attainment of systems lacking large crystallites and with an average nanoparticle size of 2 nm for both Ni and Ru (Figures S12 and S13), resulting in a metal dispersion of 48 and 56%, respectively (Figure S14). Notably, for the Ru- and Ni-based systems, selectivity patterns as well as CH_2Br_2 conversion remained unchanged (Figure S14). Consequently, the TOF values of Ni/SiO_2-NC and Ru/SiO_2-NC were lower than those of Ni/SiO_2 and Ru/SiO_2, thereby stressing the outstanding hydrodebromination activity attained over Pt/SiO_2 (Figure 11a). Moreover, these results suggest that activity over Ni- and Ru-based systems is structure dependent. The impact of active phase nanostructuring on CH_2Br_2 hydrodebromination performance deserves attention in future dedicated studies.

Further insights were gained by conducting kinetic analysis over the three systems, showing differences in the apparent activation energies with values of 53 kJ mol^{-1} (Ru/SiO_2), 36 kJ mol^{-1} (Ni/SiO_2), and 34 kJ mol^{-1} (Pt/SiO_2) (Figure 11b). On the other hand, similarities in the derived partial orders with respect to CH_2Br_2 were found, with values ranging between 1.05 and 1.21 (Figure 11c). Particularly interesting are the relatively low reaction orders in H_2 for Ni/SiO_2 and Ru/SiO_2 of *ca.* 0.47, deviating from that of a system that mainly produces CH_4, which exhibited a partial order of 1.01 (Figure 11d). These kinetic fingerprints are a direct consequence of the observed patterns described in the reaction profiles (Figures 3 and S2). For the reactant, the reaction order is around 1, which is in line with the stoichiometric term in the general equation. The same applies to the H_2 dependencies, where the production of CH_4 results in a partial order of *ca.* 1 if the reaction of the second H-atom is considered as rate determining (Figure 2). On the other hand, the production of CH_3Br requires a single H-atom and therefore shows the observed partial order in H_2 of *ca.* 0.5. Comparable results were found over nanostructured catalysts for selective CH_2Cl_2 hydrodechlorination, where a kinetic model could give an account of the possible origin of the observed selectivity differences.[14] The effects of inlet partial pressures of CH_2Br_2 and H_2 were further studied to determine the effect of these compounds on product distribution (Figure 12). Therein, adjusting the CH_2Br_2 inlet partial pressure showed a little influence on the selectivity patterns. On the other hand, changing the partial pressure of H_2 from 6 to 72 kPa had a significant effect on product distributions and activity. With increasing H_2 concentration in the feed, a higher selectivity to CH_3Br was obtained over Ru/SiO_2 and Ni/SiO_2. In contrast, a slight decrease of CH_3Br selectivity at the expense of CH_4 formation was observed over Rh/SiO_2 and Pt/SiO_2. Over all systems, coke formation was curbed at the expense of the production of either CH_3Br or CH_4 with increasing H_2 partial pressures.

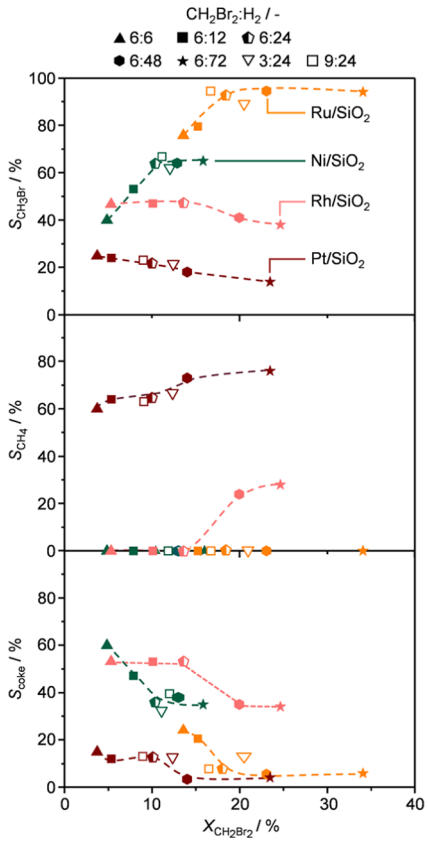

Figure 12. Selectivity to CH_3Br, CH_4, and coke in CH_2Br_2 hydrodebromination as a function of CH_2Br_2 conversion over selected catalysts. The shape and interior of the symbols provide information on the feed composition. Each catalytic data point was gathered using materials in a fresh form to exclude the possible influence of catalyst deactivation. Reaction conditions: $CH_2Br_2/H_2/Ar/He$ = 3−9:6−72:4.5:17.5−83.5, F_T/W_{cat} = 40 200 cm^3 min^{-1} g_{cat}^{-1}, T = 523 K, P = 1 bar, and tos = 0.25 h.

4. CONCLUSIONS

A strategy combining computational techniques and catalyst testing was devised with the aim to understand the performance of selected metal catalysts in the hydrodebromination of CH_2Br_2 to CH_3Br. Here, we have derived a consistent catalytic data set comprising experimentally obtained and DFT data for the application of statistical techniques. The steady-state catalytic tests of metals supported on SiO_2 revealed four performance groups comprising (i) poorly active Fe, Co, Cu, and Ag; (ii) Rh and Ni, which show intermediate selectivity to CH_3Br (<60%) but do not generate CH_4; (iii) Ir and Pt, which mainly produce CH_4 (>50%); and (iv) Ru, which exhibits the highest selectivity to CH_3Br (>96%). DFT was applied to retrieve the energy profiles over the metals, after which the binding energies of the 272 intermediates were subjected to dimensionality reduction *via* principal component analysis, a robust mathematical construct. The two descriptors obtained from this unsupervised method were, together with the experimental data, employed in the random forest regressor and the Bayesian machine scientist, ultimately connecting the descriptor energy intervals with catalytic activity or selectivity and obtaining the functional forms for the identification of performance trends in terms of CH_3Br yield. This work addresses important aspects in machine-learning-aided research, mainly (i) the use of integrated and complementary experimental and computational first-principles results, (ii) the identification of hot activity/selectivity spots through robust mathematically and nonbiased methodologies, and (iii) extraction of physically meaningful mathematical expressions to describe the performance of the catalytic systems. Ideally, these methodologies shall be able to identify new candidates and verify them experimentally. In practice, synthetic methods for different metals can end up producing different species. Therefore, the particular active site speciation, nanoparticle size, coordination, and existence of nonremoved ligands could affect the final performance and would require a much more dedicated analysis and a better understanding of the synthetic protocols. However, our approach lays the foundations for future studies targeting the full ab initio prediction of catalytic performance.

■ ASSOCIATED CONTENT

Assessment of the absence of extraparticle and intraparticle mass-transfer limitations; elementary steps of catalyzed CH_2Br_2 hydrodebromination; reaction barriers, reaction energies, and adsorption energies; imaginary vibrational frequencies; reaction energies for the $C_{hcp} \rightarrow C_{subsurface}$ reaction; energy profiles for CH_2Br_2 hydrodebromination; comparison between the two main components obtained using PCA analysis and the DFT adsorption energies of Br_{hcp} and CH_{hcp}; ratio and difference between the DFT adsorption energies of Br_{hcp} and CH_{hcp}; H_2-TPR profiles of the SiO_2-supported metal oxides; conversion of CH_2Br_2 as a function of temperature and product selectivity as a function of CH_2Br_2 conversion; accuracy with the training set for various random forest regressors containing a different number of trees; schematic representation of a BMS tree; sum of squared errors (SSE), mean squared error (MSE), root MSE (RMSE), fitting functions, and fitting constants; comparison between the calculated and experimental data using the CH_3Br selectivity fitting function; stability tests; XRD patterns, HAADF-STEM micrographs, and derived particle size distributions of the noncalcined catalysts; CH_2Br_2 conversion, product selectivity, and turnover frequency over the noncalcined catalysts (PDF)

■ AUTHOR INFORMATION

Corresponding Authors

N. López − *Institute of Chemical Research of Catalonia, ICIQ, The Barcelona Institute of Science and Technology, 43007 Tarragona, Spain;* orcid.org/0000-0001-9150-5941; Email: nlopez@iciq.es

J. Pérez-Ramírez − *Department of Chemistry and Applied Biosciences, Institute for Chemical and Bioengineering, ETH Zurich, 8093 Zurich, Switzerland;* orcid.org/0000-0002-5805-7355; Email: jpr@chem.ethz.ch

Authors

A. J. Saadun − *Department of Chemistry and Applied Biosciences, Institute for Chemical and Bioengineering, ETH Zurich, 8093 Zurich, Switzerland*

S. Pablo-García − *Institute of Chemical Research of Catalonia, ICIQ, The Barcelona Institute of Science and Technology, 43007 Tarragona, Spain*

V. Paunović − *Department of Chemistry and Applied Biosciences, Institute for Chemical and Bioengineering, ETH Zurich, 8093 Zurich, Switzerland;* orcid.org/0000-0001-6630-1672

Q. Li − *Institute of Chemical Research of Catalonia, ICIQ, The Barcelona Institute of Science and Technology, 43007 Tarragona, Spain;* orcid.org/0000-0001-5568-2334

A. Sabadell-Rendón − *Institute of Chemical Research of Catalonia, ICIQ, The Barcelona Institute of Science and Technology, 43007 Tarragona, Spain*

K. Kleemann − *Department of Chemistry and Applied Biosciences, Institute for Chemical and Bioengineering, ETH Zurich, 8093 Zurich, Switzerland*

F. Krumeich − *Department of Chemistry and Applied Biosciences, Institute for Chemical and Bioengineering, ETH Zurich, 8093 Zurich, Switzerland;* orcid.org/0000-0001-5625-1536

Complete contact information is available at: https://pubs.acs.org/10.1021/acscatal.0c00679

Author Contributions

[§]A.J.S. and S.P.-G. contributed equally to this work.

Notes

The authors declare no competing financial interest.

■ ACKNOWLEDGMENTS

This work was supported by the ETH Research Grant ETH-43 181 and Ministerio de Ciencia, Innovación y Universidades (No. RTI2018-101394-B100). The authors thank BSC-RES for generously providing computational resources. The authors thank the Scientific Center for Optical and Electron Microscopy, (ScopeM) and Prof. R. Spolenak of ETH Zurich for the use of their facilities and Raman spectroscopy, respectively. Dr. R. Hauert is acknowledged for assistance with XPS measurements. The authors thank M. J. Saadun, Profs. R. Guimerà, and M. Sales for discussions on statistical learning.

■ REFERENCES

(1) McFarland, E. Unconventional Chemistry for Unconventional Natural Gas. *Science* **2012**, *338*, 340−342.

(2) Horn, R.; Schlögl, R. Methane Activation by Heterogeneous Catalysis. *Catal. Lett.* **2015**, *145*, 23−39.

(3) Lunsford, J. H. Catalytic Conversion of Methane to more useful Chemicals and Fuels: a Challenge for the 21st Century. *Catal. Today* **2000**, *63*, 165−174.

(4) Tang, P.; Zhu, Q.; Wu, Z.; Ma, D. Methane Activation: the Past and Future. *Energy Environ. Sci.* **2014**, *7*, 2580−2591.

(5) Lin, R.; Amrute, A. P.; Pérez-Ramírez, J. Halogen-Mediated Conversion of Hydrocarbons to Commodities. *Chem. Rev.* **2017**, *117*, 4182−4247.

(6) Lange, J.-P.; Tijm, P. Processes for Converting Methane to Liquid Fuels: Economic Screening through Energy Management. *Chem. Eng. Sci.* **1996**, *51*, 2379−2387.

(7) Zichittella, G.; Paunovic′, V.; Amrute, A. P.; Pérez-Ramírez, J. Catalytic Oxychlorination versus Oxybromination for Methane Functionalization. *ACS Catal.* **2017**, *7*, 1805−1817.

(8) Paunović, V.; Zichittella, G.; Moser, M.; Amrute, A. P.; Pérez-Ramírez, J. Catalyst design for Natural-Gas Upgrading through Oxybromination Chemistry. *Nat. Chem.* **2016**, *8*, 803−809.

(9) Paunović, V.; Lin, R.; Scharfe, M.; Amrute, A. P.; Mitchell, S.; Hauert, R.; Pérez-Ramírez, J. Europium Oxybromide Catalysts for efficient Bromine Looping in Natural Gas Valorization. *Angew. Chem., Int. Ed.* **2017**, *56*, 9791−9795.

(10) Paunović, V.; Hemberger, P.; Bodi, A.; López, N.; Pérez-Ramírez, J. Evidence of Radical Chemistry in Catalytic Methane Oxybromination. *Nat. Catal.* **2018**, *1*, 363−370.

(11) Nilsen, M. H.; Svelle, S.; Aravinthan, S.; Olsbye, U. The Conversion of Chloromethane to Light Olefins over SAPO-34: The Influence of Dichloromethane Addition. *Appl. Catal., A* **2009**, *367*, 23−31.

(12) Paunović, V.; Pérez-Ramírez, J. Catalytic Halogenation of Methane: a Dream Reaction with Practical Scope? *Catal. Sci. Technol.* **2019**, *9*, 4515−4530.

(13) Lorkovic, I. M.; Sun, S.; Gadewar, S.; Breed, A.; Macala, G. S.; Sardar, A.; Cross, S. E.; Sherman, J. H.; Stucky, G. D.; Ford, P. C. Alkane Bromination Revisited: "Reproportionation" in Gas-Phase Methane Bromination Leads to Higher Selectivity for CH_3Br at Moderate Temperatures. *J. Phys. Chem. A* **2006**, *110*, 8695−8700.

(14) Saadun, A. J.; Zichittella, G.; Paunović, V.; Markaide-Aiastui, B. A.; Mitchell, S.; Pérez-Ramírez, J. Epitaxially Directed Iridium Nanostructures on Titanium Dioxide for the Selective Hydrodechlorination of Dichloromethane. *ACS Catal.* **2020**, *10*, 528−542.

(15) Ding, K.; Derk, A. R.; Zhang, A.; Hu, Z.; Stoimenov, P.; Stucky, G. D.; Metiu, H.; McFarland, E. W. Hydrodebromination and Oligomerization of Dibromomethane. *ACS Catal.* **2012**, *2*, 479−486.

(16) Vilé, G.; Albani, D.; Almora-Barrios, N.; López, N.; Pérez-Ramírez, J. Advances in the Design of Nanostructured Catalysts for Selective Hydrogenation. *ChemCatChem* **2016**, *8*, 21−33.

(17) Mäki-Arvela, P.; Hájek, J.; Salmi, T.; Murzin, D. Y. Chemoselective Hydrogenation of Carbonyl Compounds over Heterogeneous Catalysts. *Appl. Catal., A* **2005**, *292*, 1−49.

(18) Williams, T.; McCullough, K.; Lauterbach, J. A. Enabling Catalyst Discovery through Machine Learning and High-Throughput Experimentation. *Chem. Mater.* **2020**, *32*, 157−165.

(19) Serra, J. M.; Chica, A.; Corma, A. Development of a Low Temperature Light Paraffin Isomerization Catalysts with Improved Resistance to Water and Sulphur by Combinatorial Methods. *Appl. Catal., A* **2003**, *239*, 35−42.

(20) Corma, A.; Serra, J. M.; Serna, P.; Valero, S.; Argente, E.; Botti, V. Optimisation of Olefin Epoxidation Catalysts with the Application of High-Throughput and Genetic Algorithms Assisted by Artificial Neural Networks (Softcomputing Techniques). *J. Catal.* **2005**, *229*, 513−524.

(21) Holena, M.; Cukic, T.; Rodemerck, U.; Linke, D. Optimization of Catalysts using Specific, Description-Based Genetic Algorithms. *J. Chem. Inf. Model.* **2008**, *48*, 274−282.

(22) Holeňa, M.; Baerns, M. Feedforward Neural Networks in Catalysis: a Tool for the Approximation of the Dependency of Yield on Catalyst Composition, and for Knowledge Extraction. *Catal. Today* **2003**, *81*, 485−494.

(23) Rodemerck, U.; Baerns, M.; Holena, M.; Wolf, D. Application of a Genetic Algorithm and a Neural Network for the Discovery and Optimization of New Solid Catalytic Materials. *Appl. Surf. Sci.* **2004**, *223*, 168−174.

(24) Corma, A.; Serra, J. M.; Argente, E.; Botti, V.; Valero, S. Application of Artificial Neural Networks to Combinatorial Catalysis: Modeling and Predicting ODHE Catalysts. *ChemPhysChem* **2002**, *3*, 939−945.

(25) Huang, K.; Chen, F.-Q.; Lü, D.-W. Artificial Neural Network-Aided Design of a Multi-Component Catalyst for Methane Oxidative Coupling. *Appl. Catal., A* **2001**, *219*, 61−68.

(26) Hou, Z.-Y.; Dai, Q.; Wu, X.-Q.; Chen, G.-T. Artificial Neural Network Aided Design of Catalyst for Propane Ammoxidation. *Appl. Catal., A* **1997**, *161*, 183−190.

(27) Zavyalova, U.; Holena, M.; Schlögl, R.; Baerns, M. Statistical Analysis of Past Catalytic Data on Oxidative Methane Coupling for New Insights into the Composition of High-Performance Catalysts. *ChemCatChem* **2011**, *3*, 1935−1947.

(28) Pérez-Ramírez, J.; López, N. Strategies to Break Linear Scaling Relationships. *Nat. Catal.* **2019**, *2*, 971−976.
(29) García-Muelas, R.; López, N. Statistical Learning goes Beyond the *d*-Band Model providing the Thermochemistry of Adsorbates on Transition Metals. *Nat. Commun.* **2019**, *10*, No. 4687.
(30) Lakuntza, O.; Besora, M.; Maseras, F. Searching for Hidden Descriptors in the Metal-Ligand Bond through Statistical Analysis of Density Functional Theory (DFT) Results. *Inorg. Chem.* **2018**, *57*, 14660−14670.
(31) Andersen, M.; Levchenko, S. V.; Scheffler, M.; Reuter, K. Beyond Scaling Relations for the Description of Catalytic Materials. *ACS Catal.* **2019**, *9*, 2752−2759.
(32) Carberry, J. J. In *Catalysis: Science and Technology*; Anderson, J. R.; Boudart, M., Eds.; Springer: Berlin, Heidelberg, 1987; Vol. *8*, pp 1−262.
(33) Mears, D. E. Diagnostic Criteria for Heat Transport Limitations in Fixed Bed Reactors. *J. Catal.* **1971**, *20*, 127−131.
(34) Kresse, G.; Furthmüller, J. Efficiency of Ab-Initio Total Energy Calculations for Metals and Semiconductors using a Plane-Wave Basis Set. *Comput. Mater. Sci.* **1996**, *6*, 15−50.
(35) Kresse, G.; Furthmüller, J. Efficient Iterative Schemes for Ab Initio Total-Energy Calculations using a Plane-Wave Basis Set. *Phys. Rev. B* **1996**, *54*, 11169−11186.
(36) Perdew, J. P.; Burke, K.; Ernzerhof, M. Generalized Gradient Approximation Made Simple. *Phys. Rev. Lett.* **1996**, *77*, 3865−3868.
(37) Monkhorst, H. J.; Pack, J. D. Special Points for Brillouin-Zone Integrations. *Phys. Rev. B* **1976**, *13*, 5188−5192.
(38) Kresse, G.; Joubert, D. From Ultrasoft Pseudopotentials to the Projector Augmented-Wave Method. *Phys. Rev. B* **1999**, *59*, 1758−1775.
(39) Blöchl, P. E. Projector Augmented-Wave Method. *Phys. Rev. B* **1994**, *50*, 17953−17979.
(40) Grimme, S.; Ehrlich, S.; Goerigk, L. Effect of the Damping Function in Dispersion Corrected Density Functional Theory. *J. Comput. Chem.* **2011**, *32*, 1456−1465.
(41) Almora-Barrios, N.; Carchini, G.; Błoński, P.; López, N. Costless Derivation of Dispersion Coefficients for Metal Surfaces. *J. Chem. Theory Comput.* **2014**, *10*, 5002−5009.
(42) Makov, G.; Payne, M. C. Periodic Boundary Conditions in Ab Initio Calculations. *Phys. Rev. B* **1995**, *51*, 4014−4022.
(43) Henkelman, G.; Jónsson, H. Improved Tangent Estimate in the Nudged Elastic Band Method for Finding Minimum Energy Paths and Saddle Points. *J. Chem. Phys.* **2000**, *113*, 9978−9985.
(44) Henkelman, G.; Uberuaga, B. P.; Jónsson, H. A Climbing Image Nudged Elastic Band Method for Finding Saddle Points and Minimum Energy Paths. *J. Chem. Phys.* **2000**, *113*, 9901−9904.
(45) Heyden, A.; Bell, A. T.; Keil, F. J. Efficient Methods for Finding Transition States in Chemical Reactions: Comparison of Improved Dimer Method and Partitioned Rational Function Optimization Method. *J. Chem. Phys.* **2005**, *123*, No. 224101.
(46) Henkelman, G.; Jónsson, H. A Dimer Method for Finding Saddle Points on High Dimensional Potential Surfaces Using only First Derivatives. *J. Chem. Phys.* **1999**, *111*, 7010−7022.
(47) Álvarez-Moreno, M.; de Graaf, C.; López, N.; Maseras, F.; Poblet, J. M.; Bo, C. Managing the Computational Chemistry Big Data Problem: The ioChem-BD Platform. *J. Chem. Inf. Model.* **2015**, *55*, 95−103.
(48) Pablo-García, S. CH_2Br_2 Dataset. ioChem-BD Computational Chemistry Datasets, 2020.
(49) Pablo-García, S. CH_2Br_2 Additional Dataset. ioChem-BD Computational Chemistry Datasets, 2020.
(50) Hastie, T.; Tibshirani, R.; Friedman, J. *The Elements of Statistical Learning: Data Mining, Inference, and Prediction*; Springer Science & Business Media, 2009; pp 587−602.
(51) Tin Kam, H. In *Random Decision Forests*, Proceedings of 3rd International Conference on Document Analysis and Recognition, 1995; Vol. *1* pp 278−282.
(52) Abild-Pedersen, F.; Greeley, J.; Studt, F.; Rossmeisl, J.; Munter, T. R.; Moses, P. G.; Skúlason, E.; Bligaard, T.; Nørskov, J. K. Scaling Properties of Adsorption Energies for Hydrogen-Containing Molecules on Transition-Metal Surfaces. *Phys. Rev. Lett.* **2007**, *99*, No. 016105.
(53) Falsig, H.; Hvolbæk, B.; Kristensen, I. S.; Jiang, T.; Bligaard, T.; Christensen, C. H.; Nørskov, J. K. Trends in the Catalytic CO Oxidation Activity of Nanoparticles. *Angew. Chem., Int. Ed.* **2008**, *47*, 4835−4839.
(54) Bruix, A.; Margraf, J. T.; Andersen, M.; Reuter, K. First-Principles-Based Multiscale Modelling of Heterogeneous Catalysis. *Nat. Catal.* **2019**, *2*, 659−670.
(55) Guimerà, R.; Reichardt, I.; Aguilar-Mogas, A.; Massucci, F.; Miranda, M.; Pallarès, J.; Sales-Pardo, M. A Bayesian Machine Scientist To Aid In The Solution Of Challenging Scientific Problems. *Sci. Adv.* **2020**, *6*, No. eaav6971.
(56) Pablo-García, S.; Álvarez, M.; López, N. Turning Chemistry into Information for Heterogeneous Catalysis. *Int. J. Quantum Chem.*, in press, 2020.
(57) Galeener, F. L.; Mikkelsen, J. C.; Geils, R. H.; Mosby, W. J. The Relative Raman Cross Sections of Vitreous SiO_2, GeO_2, B_2O_3, and P_2O_5. *Appl. Phys. Lett.* **1978**, *32*, 34−36.
(58) Hardcastle, F. D.; Wachs, I. E. Raman Spectroscopy of Chromium Oxide Supported on Al_2O_3, TiO_2 and SiO_2: a Comparative Study. *J. Mol. Catal.* **1988**, *46*, 173−186.
(59) Korotcov, A. V.; Huang, Y.-S.; Tiong, K.-K.; Tsai, D.-S. Raman Ccattering Characterization of Well-Aligned RuO_2 and IrO_2 Nanocrystals. *J. Raman Spectrosc.* **2007**, *38*, 737−749.
(60) Amada, Y.; Watanabe, H.; Tamura, M.; Nakagawa, Y.; Okumura, K.; Tomishige, K. Structure of ReO_x Clusters Attached on the Ir Metal Surface in Ir−ReO_x/SiO_2 for the Hydrogenolysis Reaction. *J. Phys. Chem. C* **2012**, *116*, 23503−23514.
(61) Pérez-Robles, F.; García-Rodríguez, F. J.; Jiménez-Sandoval, S.; González-Hernández, J. Raman Study of Copper and Iron Oxide Particles Embedded in an SiO_2 Matrix. *J. Raman Spectrosc.* **1999**, *30*, 1099−1104.
(62) Owens, L.; Tillotson, T. M.; Hair, L. M. Characterization of Vanadium/Silica and Copper/Silica Aerogel Catalysts. *J. Non-Cryst. Solids* **1995**, *186*, 177−183.
(63) Lin, R.; Amrute, A. P.; Pérez-Ramírez, J. Halogen-Mediated Conversion of Hydrocarbons to Commodities. *Chem. Rev.* **2017**, *117*, 4182−4247.
(64) Wang, X.; Zhang, P.; Gao, J.; Chen, X.; Yang, H. Facile Synthesis and Magnetic Properties of Fe_3C/C Nanoparticles via a Sol−Gel Process. *Dyes Pigm.* **2015**, *112*, 305−310.
(65) Wang, X.; Zhang, S.; Li, J.; Xu, J.; Wang, X. Fabrication of Fe/Fe_3C@porous Carbon Sheets from Biomass and their Application for Simultaneous Reduction and Adsorption of Uranium(VI) from Solution. *Inorg. Chem. Front.* **2014**, *1*, 641−648.
(66) Clausen, C. A.; Good, M. L. Moessbauer and Far-Infrared Studies of Tetrahaloferrate Anions of the Type $FeCl_4$-nBr_n. *Inorg. Chem.* **1970**, *9*, 220−223.
(67) Anderson, A.; Lo, Y. W. Raman and Infrared Spectra of Crystals with the Cadmium Iodide Structure. *Spectrosc. Lett.* **1981**, *14*, 603−615.
(68) Li, Y.; Feng, Z.; Xin, H.; Fan, F.; Zhang, J.; Magusin, P. C. M. M.; Hensen, E. J. M.; van Santen, R. A.; Yang, Q.; Li, C. Effect of Aluminum on the Nature of the Iron Species in Fe-SBA-15. *J. Phys. Chem. B* **2006**, *110*, 26114−26121.
(69) Sinha, K.; Menéndez, J. First- and Second-Order Resonant Raman Scattering in Graphite. *Phys. Rev. B* **1990**, *41*, 10845−10847.
(70) Darmstadt, H.; Sümmchen, L.; Ting, J. M.; Roland, U.; Kaliaguine, S.; Roy, C. Effects of Surface Treatment on the Bulk Chemistry and Structure of Vapor Grown Carbon Fibers. *Carbon* **1997**, *35*, 1581−1585.
(71) Lázaro, M. J.; Echegoyen, Y.; Suelves, I.; Palacios, J. M.; Moliner, R. Decomposition of Methane over Ni-SiO_2 and Ni-Cu-SiO_2 Catalysts: Effect of Catalyst Preparation Method. *Appl. Catal., A* **2007**, *329*, 22−29.

(72) Freakley, S. J.; Ruiz-Esquius, J.; Morgan, D. J. The X-Ray Photoelectron Spectra of Ir, IrO_2 and $IrCl_3$ Revisited. *Surf. Interface Anal.* **2017**, *49*, 794−799.
(73) Morgan, D. J. Resolving ruthenium: XPS Studies of Common Ruthenium Materials. *Surf. Interface Anal.* **2015**, *47*, 1072−1079.
(74) Muhler, M.; Paál, Z.; Schlögl, R. XPS of Platinum in Pt/SiO_2 (Europt-1): Possibilities and Limitations of the Method. *Appl. Surf. Sci.* **1991**, *47*, 281−285.
(75) Zhu, Z.; Tao, F.; Zheng, F.; Chang, R.; Li, Y.; Heinke, L.; Liu, Z.; Salmeron, M.; Somorjai, G. A. Formation of Nanometer-Sized Surface Platinum Oxide Clusters on a Stepped Pt(557) Single Crystal Surface Induced by Oxygen: A High-Pressure STM and Ambient-Pressure XPS Study. *Nano Lett.* **2012**, *12*, 1491−1497.
(76) Katrib, A.; Stanislaus, A.; Yousef, R. M. XPS Investigations of Metal—Support Interactions in Pt/SiO_2, Ir/SiO_2 and Ir/Al_2O_3 Systems. *J. Mol. Struct.* **1985**, *129*, 151−163.
(77) Wang, C.-M.; Baer, D. R.; Bruemmer, S. M.; Engelhard, M. H.; Bowden, M. E.; Sundararajan, J. A.; Qiang, Y. Microstructure of the Native Oxide Layer on Ni and Cr-Doped Ni Nanoparticles. *J. Nanosci. Nanotechnol.* **2011**, *11*, 8488−8497.